Chemical Engineering Journal Advances 9 (2022) 100215

Contents lists available at ScienceDirect

Chemical Engineering Journal Advances

journal homepage: www.sciencedirect.com/journal/chemical-engineering-journal-advances

Classification of flow regimes using a neural network and a non-invasive ultrasonic sensor in an S-shaped pipeline-riser system

Somtochukwu Godfrey Nnabuife [a], Boyu Kuang [b,*], Zeeshan A. Rana [c], James Whidborne [d]

[a] Geo-Energy Engineering Centre, Cranfield University, Cranfield MK43 0AL, United Kingdom
[b] Centre for Computational Engineering Sciences, Cranfield University, Cranfield MK43 0AL, United Kingdom
[c] Centre for Computational Engineering Sciences, Cranfield University, Cranfield MK43 0AL, United Kingdom
[d] Dynamics Simulation and Control Group, Cranfield University, Cranfield MK43 0AL, United Kingdom

ARTICLE INFO

Keywords:
Ultrasonic sensor
Artificial Neural Network (ANN)
S-shaped riser
Discrete Wavelet Transforms (DWTs)
Power Spectral Density (PSD)

ABSTRACT

A method for classifying flow regimes is proposed that employs a neural network with inputs of extracted features from Doppler ultrasonic signals of flows using either the Discrete Wavelet Transform (DWT) or the Power Spectral Density (PSD). The flow regimes are classified into four types: annular, churn, slug, and bubbly flow regimes. The neural network used in this work is a feedforward network with 20 hidden neurons. The network comprises four output neurons, each of which corresponds to the target vector's element number. 13 and 40 inputs are used for features extracted from PSD and DWT respectively. Experimental data were collected from an industrial-scale multiphase flow facility. Using the PSD features, the neural network classifier misclassified 3 out of 31 test datasets in the classification and gave 90.3% accuracy, while only one dataset was misclassified with the DWT features, yielding an accuracy of 95.8%, thus showing the superiority of the DWT in feature extraction of flow regime classification. The approach demonstrates the applicability of a neural network and DWT for flow regime classification in industrial applications using a clamp-on Doppler ultrasonic sensor. The scheme has significant advantages over other techniques as only a non-radioactive and non-intrusive sensor is used. To the best of our knowledge, this is the first known successful attempt for the classification of liquid-gas flow regimes in an S-shape riser system using an ultrasonic sensor, PSD-DWTs features, and a neural network.

1. Introduction

Multiphase liquid-gas flows occur simultaneously inside the pipeline riser in a wide range of industrial and engineering processes, for example in nuclear energy, petrochemical and food-processing plants [1,2], as well as in chemical reactors, steam boilers and their associated process piping and condensers [3]. Two-phase flow system operations and design require accurate prediction of the system's pressure drops which is based on the proper knowledge of the type of the flow regime that is obtainable in the two-phase flow facility. Different two-phase flow regimes can occur depending on the volume fractions, velocities and fluids' properties, as well as the pipe geometry [4]. In vertical or S-shape pipeline risers, the most frequently experienced flow regimes are annular, bubbly, slug and churn flows.

Usually, the flow regime can be identified using a flow map [5]. Flow regime input parameters based on physical mechanisms are usually gas and liquid superficial velocities, that are unmeasurable during online operations [6]. Furthermore, while flow regime is influenced by many factors, only a few are considered in building the flow maps [7]. The applicability of a flow map by which experimental data are acquired from gas-liquid flows is limited. Hence, the credibility of flow regime identification using flow maps is not guaranteed.

Flow patterns can be recognised either through direct identification or indirect recognition methods [8]. Gas-liquid two-phase flow direct

Abbreviations: DWT, Discrete Wavelet Transform; SVM, Support Vector Machine; ANN, Artificial Neural Network; PSD, Power Spectral Density; CWDU, Continuous Wave Doppler Ultrasound; OPEX, Operating Expenditure; CPDF, Cumulative Probability Density Function; PDF, Probability Density Function; LabVIEW, Laboratory Virtual Instrument Engineering Workbench; SCADA, Supervisory Control and Data Acquisition; TWF, Twin-Window Feature; FFT, Fast Fourier Transformation; ROC, Receiver Operating Characteristic.

* Corresponding author.
E-mail addresses: g.nnabuife@cranfield.ac.uk (S.G. Nnabuife), neil.kuang@cranfield.ac.uk (B. Kuang), zeeshan.rana@cranfield.ac.uk (Z.A. Rana), j.f.whidborne@cranfield.ac.uk (J. Whidborne).

https://doi.org/10.1016/j.ceja.2021.100215
Received 1 September 2021; Received in revised form 11 November 2021; Accepted 17 November 2021
Available online 24 November 2021

identification with special equipment and instruments was investigated because of the limitations of the flow regime map. There are two ways to obtain flow regime direct identification: one is direct observation, for instance using a high-speed camera and adopting a visual method. This type of the flow regime classification is based on subjective means, which may vary for different observers. The other is characteristic variable extraction from a two-phase flow fluctuation signal. Direct identification methods require the operator to visually interpret the flow in order to classify it into a flow regime. This method of flow regime identification in industrial plant pipelines is complicated as the industrial fluids flow in opaque steel pipes and often at a high temperature and pressure. The indirect determination method, also known as analytical recognition, is a two-way process. First, the operator measures the flow parameter characteristics using a reliable experimental method. Then, the data is analysed objectively to determine the flow regime [9].

The direct measurement procedure is the most common and simplest method of flow regime identification. It is, however, the most subjective approach, with results being determined at the operator's discretion and hence resulting in a low level of replicability and repeatability by others. The flow transitions also complicate flow regime delineation as the progression from one flow regime to another is not instantaneous but rather develops via intermediate regimes that exhibit mixed characteristics [10]. In 1969, Hewitt and Robert proposed the use of X-rays as an extension of the light photograph but operators did not widely accept this approach. This is due to the safety requirement, the relatively long exposure times and advances in technology [11].

Statistical parameters such as void fractions were proposed as a means of flow regime identification around 1980. Using PDF in analysing this parameter allows for flow regime identification from experimental data. However, the rules regarding flow regime identification using statistical parameters are at the operator's discretion, thereby retaining the probability of subjective analysis. Hence, the objective classification of flow regime is not guaranteed [12]. The PDF approach in comparison with the use of a high-speed camera shows that PDF has a poor performance in delineating between churn and slug flow but is effective in distinguishing between annular and churn flow [13].

A noteworthy advance in the objective identification of flow regime was established by the introduction of an Artificial Neural Network (ANN) [14,15]. A more successful objective process was established by classifying the flow regime indicators acquired through non-intrusive impedance probes and a Kohonen Self-Organising Neural Network (SONN) [9]. The classification using SONN was initially carried out using the PDF of the void fraction signals as an indicator. However, this approach has a significant disadvantage in that a longer observation period is required to acquire a reasonable statistical parameter of the void fraction signal. This was later enhanced when the Cumulative Probability Density Function (CPDF) of the impedance void metre signals was introduced [16]. The CPDF proved to be more stable because it is integral and faster than the PDF methods, as it needs fewer input data. Flow regime identification adopting a fuzzy and neural network methodology has been studied. The signal variable characteristics used to depict the flow regime were obtained based on the statistical analysis method. However, the results were limited because the signal processing methods used were based on conventional linear techniques such as wavelet transform and Fourier analysis. The application and analysis of these methods based on nonlinear theory is a future research focus.

Online flow regime identification plays a vital role in many areas of the industry and in scientific investigations relating to two-phase gas-liquid flow [17]. It is established that the operation proficiency of this process is proximately related to precise measurement and the control of hydrodynamic parameters such as flow rate and flow regimes. For instance, in the subsea oil field transportation of gas-liquid flow, online flow regime identification is profitable to the refitting (modification) of operational methods and the enhancement of process proficiency. A two-phase gas-liquid cyclonic separator's modelling and redesigning can gain from the overall air core motion measurement. In the petrochemical industries, the online monitoring of gas-oil flows is vital for safe operation in the fields of production and exploration [18]. The sudden arrival of slug flows at the feed of three-phase separators installed on offshore production platforms results in severe transients to the control systems, which reduces the equipment's operating efficiency [19]. The likelihood of preventing such regimes can increase the number of information available for operators, such as industrial processes increasing the operational efficiency and security.

Flow regime identification using an ANN is reviewed with regards to its applications with electrical impedance sensors and pressure differential transducers as measuring devices. This choice is due to increasing interest in using an ANN with these measurement methods, in contrast to the use of a Support Vector Machine (SVM) [20] or an image analysis of dynamic neutron radiograph videos [21]. The benefits and drawbacks of using impedance sensors and pressure transducers as measuring devices in flow regime identification are as follows. Impedance sensors have a raw output signal that is a function of the void fraction [20]. This feature, due to being closely related to the flow regime, requires less computational effort in mapping the signal features to the flow regime. Pressure transducers are less expensive, readily available for a wide range of operating conditions, well developed and fulfil most of the operational safety regulations [20]. Electrical impedance and pressure transducers are the invasive techniques which require either direct contact with fluids making them prone to corrosion and blockage or insertion of special dielectric pipe for electrical capacitance sensors.

A Doppler ultrasonic sensor that deploys continuous wave ultrasound signals can also attain flow velocity non-intrusive measurement [22,23]. Deployment of this type of technique is already in existence in the medical field. The method deploys a shift in frequency constituting the flow velocities to develop a means of making flow regime predictions [24]. The applicability of CWDU in two-phase flow velocity measurements was investigated by [25]. They suggested the deployment of frequency resolution methods to alter the issues of velocity profile measurement by coloured noise presence, but this caused a severe problem for the classical frequency estimators.

This study proposes a non-radioactive and non-invasive approach for objectively identifying two-phase gas-liquid flow regimes using CWDU and a neural network. The objective detection of flow regimes utilising a clamped-on, non-radioactive, and non-invasive ultrasonic sensor is of significant relevance to many industries. Non-invasive and non-radioactive techniques are appealing because they eliminate the requirement for instrumentation immersion in the flow and are less expensive to develop because they do not employ radioactive materials. Moreover, the Operating Expenditure (OPEX) is less compared to radioactive instruments due to the excessive costs associated with safety, environmental and health issues [26]. The ultrasonic technique is a promising alternative to complex, hazardous and costly techniques [26, 27].

The ANNs are regarded as an alternate method for identifying objective flow regimes [20] and since the early 1980s have been employed extensively for applications such as parameter estimation, fault detection, model-based control, dynamic modelling, process monitoring and adaptive control [28]. The key contributions of this paper are as follows: (i) to develop ANNs for objective flow regime identification using Doppler ultrasonic data as input, (ii) to demonstrate that Doppler ultrasonic signals have the potential to provide reliable online information for the flow regime identification of gas-liquid two-phase flow and (iii) this also seems to be the first known successful attempt to use CWDU, PSD-DWTs features, and a neural network to objectively identify gas-liquid flow regimes in an S-shape riser.

This paper is organised as follows: Section 2 presents the measurement sensor and the algorithm, while Section 3 describes the experimental method used in this study. The signal analysis and observations are discussed in Section 4, after which Section 5 presents the results and discussion of the analysed data. Finally, Section 6 concludes on this

paper's findings.

2. The algorithm and measurement sensor

The Doppler effect is the frequency fluctuation of an acoustic wave when there is movement between the acoustic receiver and the source, and the change in frequency is proportional to the velocity of the acoustic source [29]. The velocity of the acoustic source is thus calculated by measuring the frequency shift between the acoustic receiver and the source [30]. In the ultrasonic Doppler technique, a fixed-frequency acoustic beam is released continuously from an ultrasonic transducer into the flow and the sound wave is reflected by moving the scatters [31]. The dispersed acoustic beam is received by another ultrasonic transducer, which estimates the fluid velocity using the frequency shift based on the Doppler effect [30].

The CWUD utilised in this study is a non-radioactive flowmeter that can detect reflecting ultrasonic fluid flows. It computes frequency changes, analyses ultrasonic signals, and estimates flow velocity. The CWUD estimates the frequency change of signals reflected by dispersed bubbles in the moving stream. To minimise air cavities being trapped between the sensor and the conduit surface, a glycerine gel was used to provide a sufficient bonding between the exterior conduit surface and the sensor. The CWUD contains two independent crystal transducers integrated in a single probe that send and receive ultrasonic waves at 500 KHz continuously [32].

One transducer in the CWUD contains two piezoelectric crystal components. The meter's electrical circuit continuously electrifies the transducer; one transducer produces an ultrasonic signal, while the other, the receiving transducer, gives output signals [33]. The flowmeter electronics then filter and boost the incoming output signals. The processed output signals are the Doppler frequency-shift signals, which were acquired with a LabVIEW software and a data collection card (NI-PCI-6040E) that controlled the 10 kHz sampling frequency for 900 s in each dataset.

3. Test rig and experimental procedure

3.1. The multiphase flow test facility

Cranfield University's oil and gas facility offers one of the best multiphase test facilities in the UK, similar to those used in industry. It is completely automated and uses a cutting-edge industrial standard distributed control system. The DeltaV Supervisory Control and Data Acquisition (SCADA) software from Emerson Process Management is used to control this test rig. For the test rig's schematic design see [34].

The test flow system is a fully computerised high pressure test system designed to control and metre the flow rate of liquid and gas mixtures through the fluid-metering section, the test section, and finally the separation section, where the liquid-gas mixtures are separated further into their phases. After final separation in a horizontal three-phase gravity separator, the water was cleaned in the coalescer before being returned to the repository vessel and the air being released into the atmosphere [34]. The compressed air is provided by a bank of two parallel linked compressors. When both compressors are operated in tandem, a maximum air flow rate of 1410 m^3/hr at 7 bar is possible. To prevent compressor pressure fluctuations, the air from the two compressors is collected in an 8 m^3 capacity receiver. Air from the receiver is routed through a bank of three filters (coarse, medium, and fine), and then via a cooler, where debris and condensates are removed before entering the flow metres [32]. Water flow rate was provided by a water tank with a capacity of 12.5 m^3. The multistage Grundfos CR90–5 pumps provided water to the flow system. At 10 pressure, the water pump has a duty of 100 m^3/hr. Frequency variable inverters are used to control the speed. DeltaV, a Fieldbus-based SCADA programme, is used to remotely control the water pumps. A 1-inch Rosemount 8742 magnetic flow metre (up to 7.36 l/s) and a 3-inch Foxboro CFT50 Coriolis metre (up to 30 kg/s) were used to measure the water flow rate [34].

Air and water were separated in an 11.12 m^3 horizontal three-phase gravity separator after passing through the test portion. Following separation and cleaning in the three-phase separator, air is discharged into the atmosphere, while water from the three-phase separator enters its 1.6 m^3 coalescer, where it is cleaned further before returning to the storage tank [35].

3.2. The multiphase flow loop of an S-shaped riser System

The experiment was conducted out at Cranfield University's Process System Engineering centre on a 2-inch S-shaped riser of the three-phase flow loop. A 40-metre horizontal pipeline, a 5.5-metre vertical lower portion, a 1.5-metre down-comer, a 5.7-metre vertical upper section, and a 3.5-metre topside segment make up the 2-inch flow loop. A transparent pipe in the 2-inch S-shaped flow loop test portion allows for flow regime monitoring. To obtain the required flow patterns, the air flowrate was changed via regulating the valves using the DeltaV [34].

3.3. Flow regime classification methodology

One hundred and twenty-five dataset measurements on the S-shape two-phase flow were collected and pre-processed for this work. Discrete wavelet transform and PSD were then applied to extract features from the pre-processed signals. The extracted features were randomly divided into training, validation and testing dataset in the ratio of 0.60:0.15:0.25, respectively. A feedforward neural network developed in MATLAB was applied to classify the two-phase air-water flow regimes using the extracted features. The output from the network was classified into the following flow regimes: slug flow, bubbly flow, churn flow and annular flow. If the liquid flow rate is high and the gas flow rate is low, the liquid will form a continuous phase. Small bubbles of gas circulate inside the liquid. This is the bubble flow regime. If the liquid flow rate is reduced while the gas flow rate remains relatively low, tiny gas bubbles may collapse to produce big gas bubbles. The liquid now forms a slug body with entrained tiny gas bubbles, followed by a single big gas bubble. This is known as the slug flow regime or intermittent flow [22]. If the low gas flow rate is increased while the liquid output remains low, the big gas bubbles might become unstable, resulting in chaotic movement of gas bubbles of diverse shapes and sizes. This is the churn flow regime. If the gas flow rate is raised while the liquid production rate is kept low, the flow will change to annular flow. In the pipe's core, gas will form the continuous phase, with liquid entrained as tiny droplets. A liquid film forms along the pipe wall [35]. This methodology is described in Fig. 2 and further explained in the subsequent sections.

3.4. Ultrasonic sensor data collection and pre-processing

Clamp-on non-intrusive CWUD transducer with an excitation voltage of 10 V and a frequency of 500 kHz was mounted to the topside of the S-shaped riser. On the S-shaped riser, the ultrasound beam had a 45° incidence angle with regard to the flow direction. To avoid measurement inaccuracies caused by cavitation, swirls, and turbulent eddies, the ultrasonic sensor must be placed at least 10 diameters away from the tees, valves, and bends on the flow pipe. To facilitate the transfer of ultrasonic energy, a coupling gel was placed between the pipe wall and the Doppler transducer [32]. The Doppler Ultrasonic sensor used in this paper is a commercial ultrasonic sensor produced by DFM2 Automation Ltd UK. The transducer of the sensor has two piezoelectric crystals, one for generating the sound wave and the other for receiving the ultrasound reflected by the scatterers in the fluids. The receiving transducer and the transmitting transducer are all built in one prob.

The Doppler frequency shift voltage signals were acquired using a LabVIEW data-acquisition system with a sampling frequency of 10 kHz. Finally, average flow velocity is the process variable determined by ultrasonic Doppler. Based on the flow velocity range and pipe scale, it was

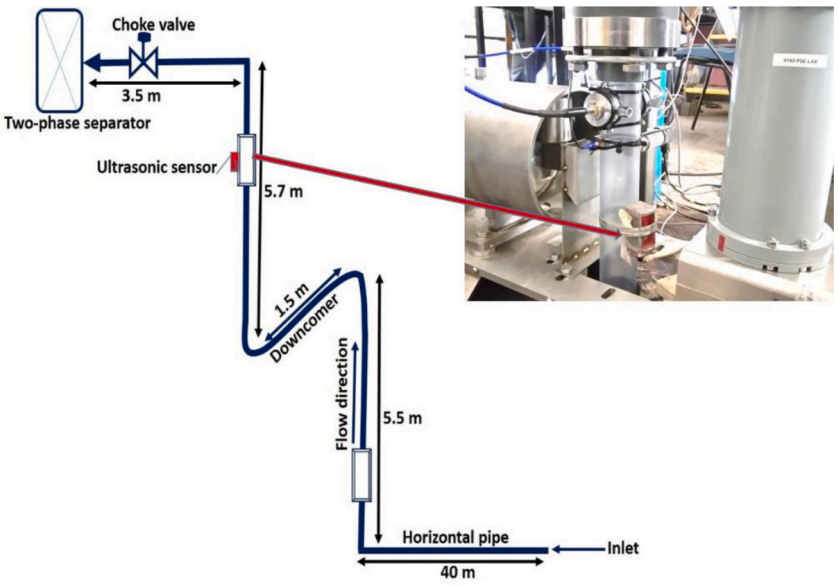

Fig. 1. S-shape rig schematic diagram [34].

Table 1
PSD frequency bands.

Band of frequencies PSD frequency bands of Doppler signal Bands	Frequency range (Hz)	Mean power
B_1	0–120	P_{B1}
B_2	120–240	P_{B2}
B3	240–360	P_{B3}
B4	360–480	P_{B4}
B5	480–600	P_{B5}
B6	600–720	P_{B6}
B7	720–840	P_{B7}
B8	840–960	P_{B8}
B9	960–1080	P_{B9}
B10	1080–1200	P_{B10}

predicted that the flow velocity fluctuates at no more than 2 kHz. With respect to the Nyquist criteria, a sampling frequency of 10 kHz is adequate in the LabVIEW data-acquisition system since it is 5 times the anticipated upper limit frequency of the flow velocity variations. Before feature extraction and flow regime classification, the data were imported into MATLAB and pre-processed [34].

3.5. Spectral analysis and feature extraction from ultrasonic Doppler signals

The input layer of the proposed ANN-based classifier includes many variables. It is noteworthy that the irrelevant variables can degrade the accuracy and computational efficiency of the classifier [36,37]. Thus, this research applies spectral analysis, power spectral density (PSD), and discrete wavelet transform (DWT) to extract relevant features instead of inputting the unprocessed data to the ANN-based classifier.

3.5.1. Spectral analysis

Spectral analysis is often used to analyse two-phase flow signals and estimate the oscillation period. The signals of a two-phase flow can be analysed from a time and frequency domain to extract the features of different flow regimes. In this study, PSD and DWT techniques were employed to extract the features of two-phase flow signals obtained using CWDU [38]. Power spectral density was applied in the analysis to obtain the periods of oscillation based on the signal Fourier transform [39]. Discrete wavelet transform has the potential of denoising and analysing the signals in order to obtain the spectrum in the frequency-time domain.

3.5.2. Power spectral density

The PSD is an approach of approximating the features of the time series signal of a stochastic method in the frequency components that are hidden in the process [40]. Features can be retrieved from either the time domain or the frequency domain for high-frequency data such as ultrasonic Doppler waves. The frequency domain PSD characteristics that are often employed in this study were utilised in this work. Several works have been done on PSD application to a time-series signal such as a pressure fluctuation signal of two-phase flow. Assuming that a discrete-time signal $x(n)$ is stationary, the PSD function $P_x(f)$ of this signal is defined as the Fourier transform of the autocorrelation sequence $R_x(k)$ [41]:

$$P_x(f) = \sum_{k=-\infty}^{\infty} R_x(k)\exp\left(-2\pi ik\,\frac{f}{f_s}\right) \tag{1}$$

where f_s denotes the sampling frequency. As the signal applied for this study is only estimated on a finite interval [0, …, $N-1$], Welch's technique for finding the PSD was used, which is given as.

$$\widehat{P}_x(f) = \sum_{k=-N+1}^{N-1} \widehat{R}_x(k)\exp\left(-2\pi ik\,\frac{f}{f_s}\right) \tag{2}$$

where the autocorrelation is [39]:

$$\widehat{R}_x(k) = \frac{1}{N}\sum_{n=0}^{N-1-k} x(n+k)x(n) \tag{3}$$

In this study, the PSD characteristics from each sample of ultrasonic Doppler signals at varied gas-liquid flow rates were analysed using Welch's technique in the same way as [41] did. One hundred twenty-five data samples with varying surface liquid and gas velocities were collected. Visual observation at the same ambient temperature settings was used to give different flow regime labels to each data sample. Each collected data sample is made up of 900 s of Doppler frequency shift signals. The dataset was divided into 60 percent for training, 15% for validation, and 25% for testing. In this study, a sample frequency of 10 kHz was used, while a Hanning window of 1024 in length and a 75 percent overlap were employed in the Welch's technique analysis Eqn. (1)–(15) [44], Figs. 1,11, Table 3.

Table 2
The frequency band range in the various wavelet decomposition levels [24].

Wavelet decomposition ranges of frequency bands		
Decomposed signals	Samples amount	Frequency range (Hz)
D_1	600,000	2500–5000
D_2	300,000	1250–2500
D_3	150,000	625–1250
D_4	75,000	312.5–625
D_5	37,500	156.25–312.5
D_6	18,750	75.125–156.25
D_7	9375	39.0625–78.125
D_8	4687.50	19.53125–39.0625
D_9	2343.75	9.765625–19.53125
D_{10}	1171.88	4.88280 - 9.765625

Table 3
Different neural network algorithms used [49,50,53].

Description	Symbols
Levenberg-Marquardt	LM
BFGS quasi-Newton	BFGS
Resilient backpropagation	Rprop
Scaled conjugate gradient	SCG
Conjugate gradient with Powell/Beale restarts	CGB
Fletcher-Powell conjugate gradient	CGF
Polak-Ribiére conjugate gradient	CGP
One step secant	OSS
Variable learning rate backpropagation	GDX

Table 4
Accuracies of each of the flow regime classification and overall accuracies of the classifiers.

Classifiers	Flow patterns	Identification accuracies (%)
ANN with PSD features	Slug flow	83.3
	Bubbly flow	100
	Churn flow	85.7
	Annular flow	100
	Total accuracy	90.3
ANN with DWT features	Slug flow	93.3
	Bubbly flow	100
	Churn flow	100
	Annular flow	100
	Total accuracy	98.6

Fig. 3 depicts typical power spectral estimates from each flow regime. The relevant frequency spectrum was found to be between 0 and 1200 Hz. The PSD spectrum is different in each flow regime in this range. As a result, the band of length 120 Hz on the spectrum was used to compute the mean PSD (PB1 – PB10) on each band (B1 – B10) to get the real characteristics that help to differentiate between the flow regimes, as shown in Table 1. Furthermore, for each sample, the maximum peak of the PSD, the weighted mean frequency $\bar{f}$ of the spectral power and the spectral power variance equation σ_f^2 were computed [35]. And finally, we have .

$$\bar{f} = \frac{\sum_i f_i P_x(f_i)}{\sum_i P_x(f_i)} \tag{4}$$

$$\sigma_f^2 = \frac{\sum_i (f_i - \bar{f})^2 P_x(f_i)}{\sum_i P_x(f_i)}. \tag{5}$$

The power spectrum of ultrasound waves yielded 13 characteristics in total: the mean PSD for each of the 10 frequency bands, as indicated in Table 1, the greatest peak of the PSD, $\bar{f}$ and σ_f^2. This method is widely used to differentiate each flow regime by utilising frequency domain characteristics [41,42]. Abbagoni and Hoi [41] utilised a similar approach on a different riser system, the horizontal pipeline-riser system, which is worth noting. Abbagoni and Hoi [41] stated that the PSD spectrum was obtained from a signal with a frequency band of 0–600 Hz using an ultrasonic Doppler sensor, but this study used a wider band of 0–1200 Hz. A wider band implies that the signal can hold more information, which will help it deal with the issue of the S-shaped riser. These features were further visualised in 2-dimensional space using PSD, before classification by the neural network, as shown in Fig. 3. The liquid and gas flow rates of all samples from the experiment are shown in Fig. 4.

3.5.3. The discrete wavelet transform

The DWT input decompose signals into sub-bands with smaller bandwidths and slower sample rates. The application of signal decomposition using DWT is not new. However, its applicability is based on the capability to regulate the wavelet coefficients in order to recognise the signal characteristic that distinguishes them from the raw time signal [43]. In this study, the decomposition of Doppler ultrasound signals from a two-phase flow was evaluated using DWT.

The signal was decomposed by wavelet transform into a set of wavelets bases. These basis functions are obtained by the contractions,

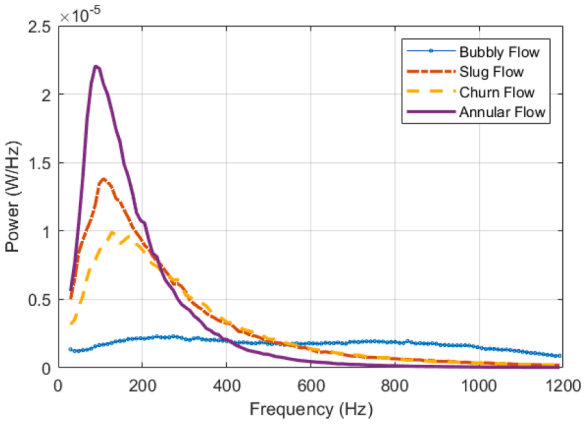

Fig. 3. Typical power spectra of each flow regime [35].

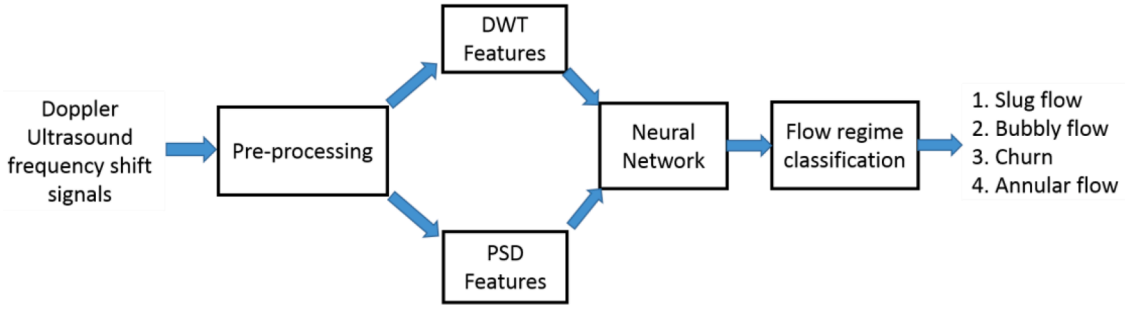

Fig. 2. Techniques for determining objective flow regimes.

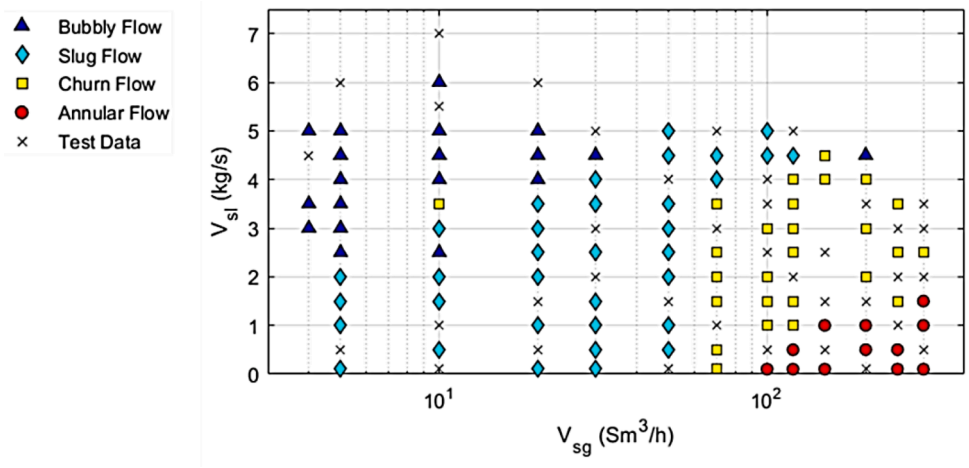

Fig. 4. The samples liquid and gas flow rates from the experiment [35].

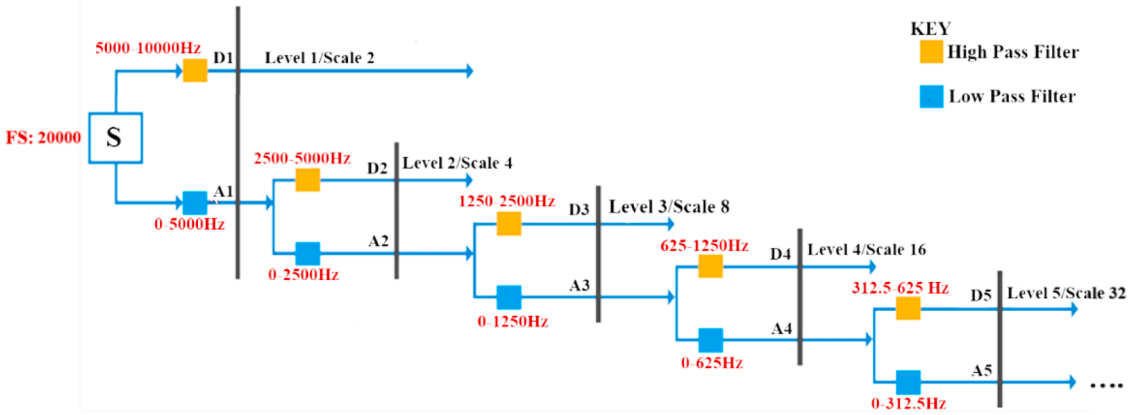

Fig. 5. Sub-band decomposition of DWT.

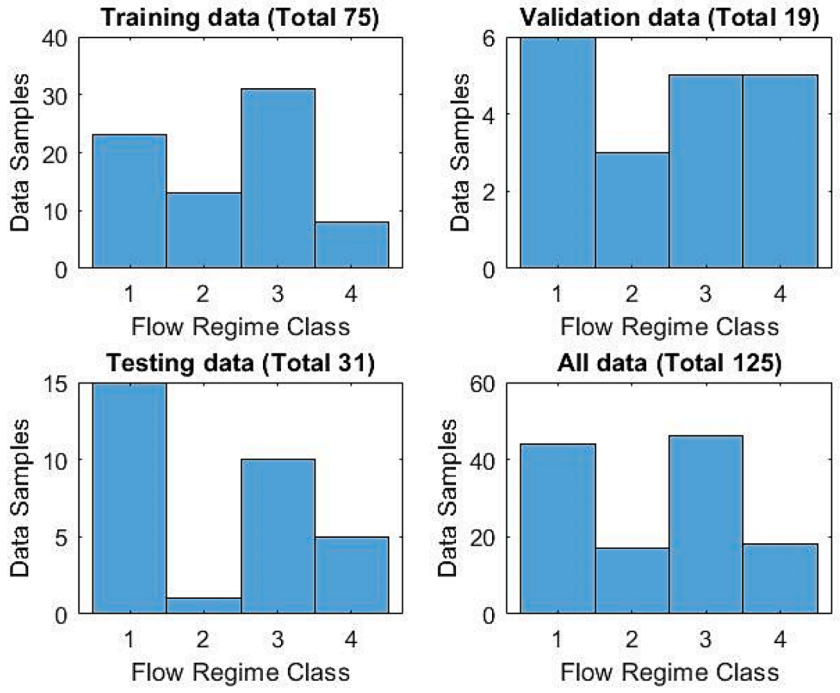

Fig. 6. Distribution of experimental, testing and training datasets for DWT.

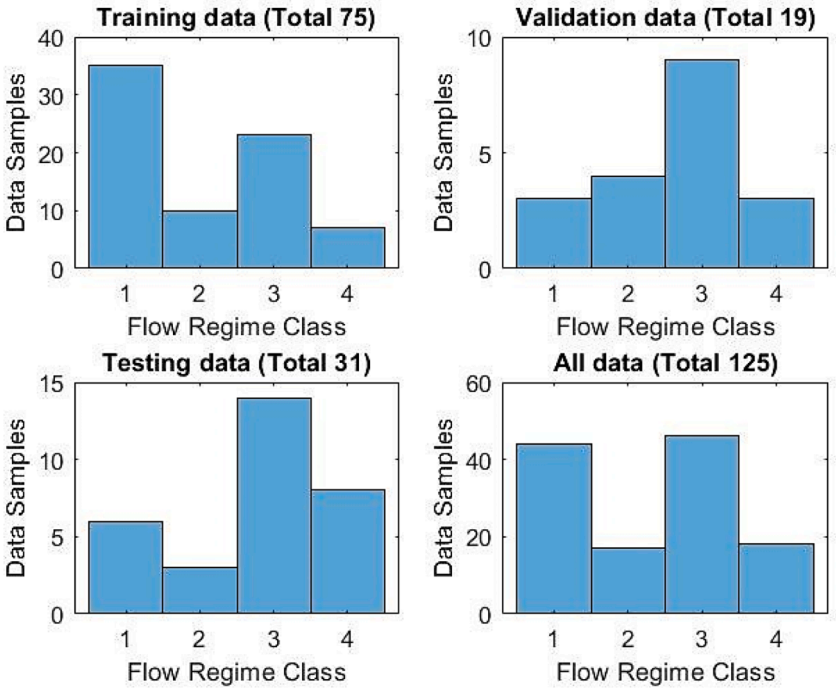

Fig. 7. Distribution of experimental, testing and training datasets for PSD.

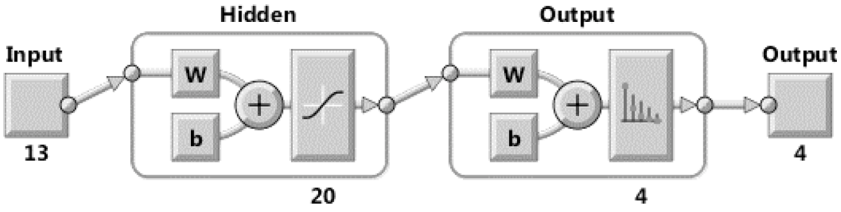

Fig. 8. Feedforward neural network with 13 input features from PSD.

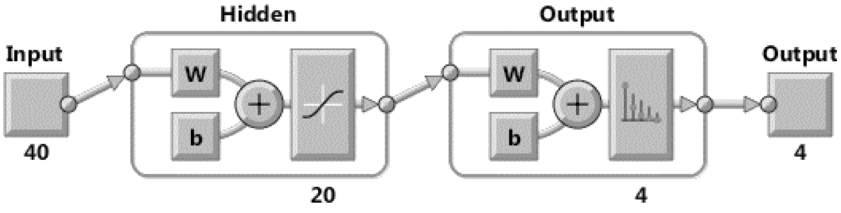

Fig. 9. A two-level feedforward neural network with 40 input features from DWT.

dilations and shifts of a unique function called wavelet prototype. Continuous wavelets are functions generated from a single function ψ by translations and dilations [44,45].

$$\psi_{a,b}(t) = \frac{1}{\sqrt{|\mathbf{a}|}}\psi\left(\frac{t-b}{a}\right) \tag{6}$$

where b is a real-valued function called the shift parameter. The function set ($\psi_{a,b}(t)$) is known as a wavelet family. As the parameters (a, b) are continuous-valued parameters, the transform is called continuous wavelet transform. Classical wavelets as dilates of one function are defined as high-frequency wavelets with a width corresponding to $a < b$ or narrower, while low-frequency wavelets have a width of $a > 1$ or wider. The wavelet transform f(t) is defined as a linear combination of wavelet and scaling wavelet functions. Both the wavelet and scaling functions are complete sets [45]. Generally, the shift and scale parameters of the discreet wavelet family are given by

$$a = a_0^j,\ b = kb_0a_0^j \tag{7}$$

where k and j are integers. The function family with discretized parameters is given as

$$\psi_{j,k}(t) = a_0^{-\frac{j}{2}}\psi\left(a^{-j}t - kb_0\right) \tag{8}$$

$\psi_{j,k}(t)$ is known as DWT basis. Even though it is known as DWT, the time variable of the transform is still continuous. The DWT coefficients of a continuous time function are expressed as

$$d_{j,k} = \left\langle f_w(t),\ \psi_{j,k}(t)\right\rangle = \frac{1}{a_0^{j/2}}\int f_w(t)\psi\left(a_0^{-j}t - kb_0\right)dt \tag{9}$$

When the DWT set ($\psi_{j,k}(t)$) is complete, the wavelet representation of a function $f_w(t)$ is defined as

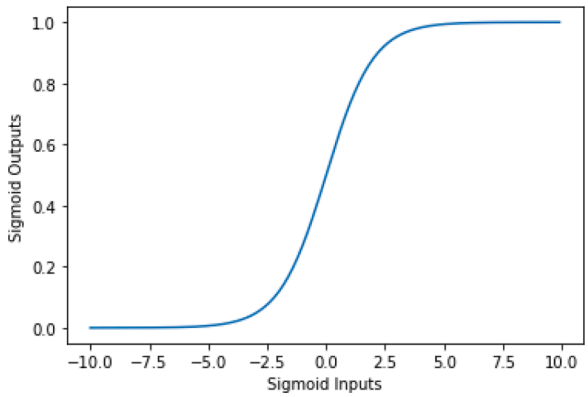

Fig. 10. The distribution of the Sigmoid activation for the hidden layer. The inputs are more different from zero, the response is weaker.

$$f_w(t) = \sum_j \sum_k \langle f_w(t), \psi_{j,k}(t) \rangle \psi_{j,k}(t) \tag{10}$$

Generally, a function can be represented by using L-finite resolutions of the wavelet and the scaling function with a parameter value of$a_0 = 2$ and $b_0 = 1$ as

$$f_w(t) = \sum_{k=-\infty}^{\infty} C_{L,k}\, 2^{-\frac{L}{2}} \varphi\left(2^{L} - k\right) + \sum_{j=1}^{L} \sum_{k=-\infty}^{\infty} d_{j,k}\, 2^{-\frac{j}{2}} \varphi\left(2^{j} - k\right) \tag{11}$$

where scaling coefficients [$C_{L,k}$] are expressed as

$$C_{L,k} = \langle f_w(t),\ \psi_{L,k}(t) \rangle = \int f_w(t) 2^{-\frac{L}{2}} \varphi\left(2^{L} - k\right) dt \tag{12}$$

and

$$\varphi_{L,k}(t) = 2^{-\frac{L}{2}} \varphi\left(2^{-L} t - k\right) \tag{13}$$

$$\psi = 2\sum_k h_1(\mathrm{k}) \varphi(2t - k) \tag{14}$$

$$\varphi = 2\sum_k h_0(\mathrm{k}) \varphi(2t - k) \tag{15}$$

3.5.3.1. Multi-resolution decomposition of Doppler ultrasound signals. Discrete wavelet transform analyses the Doppler signal at different frequency bands and with different resolutions by decomposing the Doppler signal into a coarse approximation and detailed information. It uses two sets of functions called wavelet functions and scaling functions, which are associated with high-pass and low-pass filters, respectively. The decomposition of the signal into the different frequency bands is obtained by successive low-pass and high-pass filtering of the time-domain signal.

The original signal (S) is first passed through a half band high-pass filter and a low-pass filter. After the signal filtering, half of the signal samples can be removed as indicated by the Nyquist criteria, as the signal at this point has the highest frequency of π/2 radians, instead of π [46]. The signal can therefore be divided into two sub-samples by simply discarding every other sample. This process is called the multi-resolution decomposition of a signal and is schematically shown in Fig. 5: Sub-band decomposition of Each stage in this scheme consists of two digital filters and two factor-of-two down-samplers. The discrete mother wavelet is the first filter, which is high-pass in nature, and the second is its mirror version, which is low-pass in nature. The down-sampled outputs of the first high-pass and low-pass filters provide the detail D_1 and the approximation A_1, respectively. The first approximation, A_1, is further decomposed and this process is continued as shown in Fig. 5.

The signals decomposition provides detail and approximation levels, with different frequency bands employing successive high-pass and low-pass filtering. In the time domain, these detail levels do not lose their information [47]. However, valuable data can be acquired from the

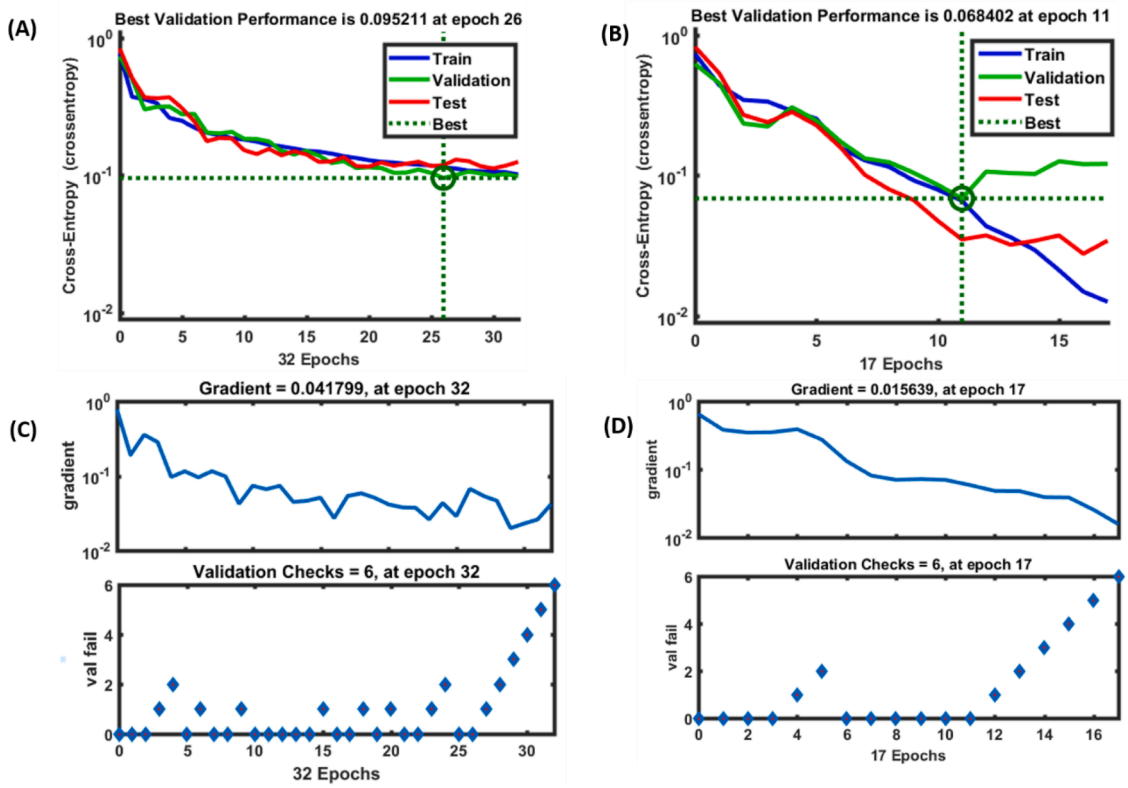

Fig. 11. . The best validation performance of the network using PSD- and DWT-extracted features is represented in Plots A and B, respectively.

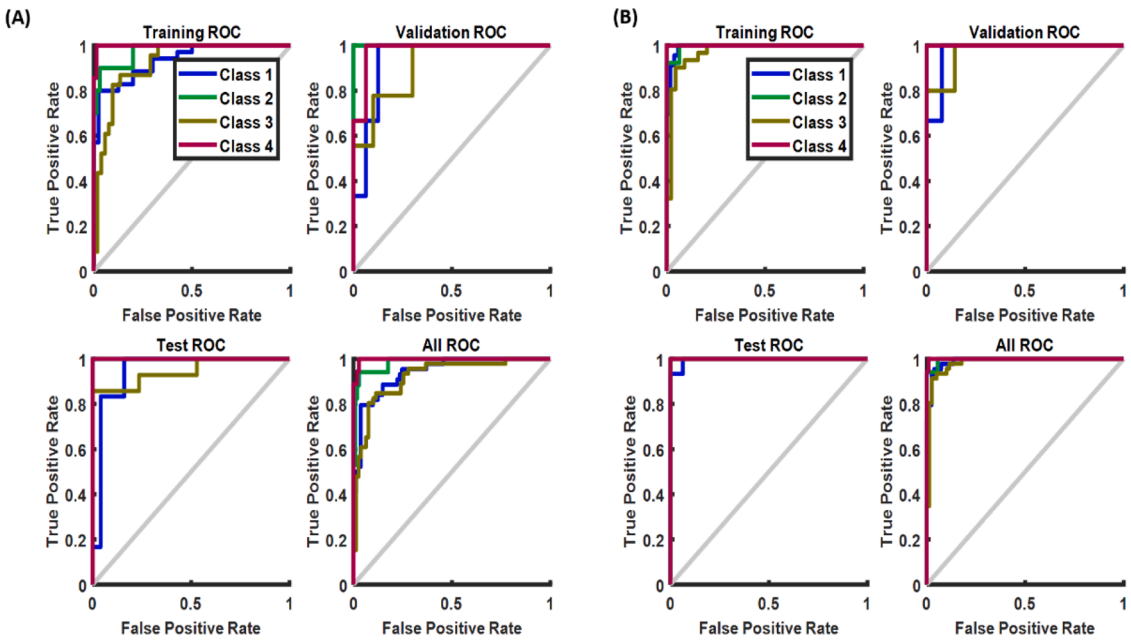

Fig. 12. The receiver operating characteristic curve for PSD and DWT.

sub-bands of the dominant frequencies. Hence, the statistical capacities of the sub-bands represent these detail levels. The flow signals were decomposed continuously until all the dominant frequency ranges were viewed. The Doppler ultrasound signal was decomposed into the detail coefficients of $D1$–D_{10}, where 1–10 is the detail wavelet coefficients levels [41].

In this work, the Doppler ultrasonic signal was decomposed into the detail coefficients of $D1-D10$, where 1–10 refers to the detail wavelet coefficient levels: the first to the seventh and the last approximations are $\_A10$. The frequency sub-band ranges are given in Table 2. The fourth-order Daubechies wavelet (db4) was deployed inorder to calculate the signal's wavelet coefficients [41]. The coefficient's DWT was computed using the MATLAB software package. For each of the datasets, detail wavelet coefficients at the first level, second level and up to the tenth level were computed. Primarily, in order to reduce the size of the feature extracted from the coefficients, statistical measurements were applied to the values of $D1$ to $D10$, as in [24]:

(a) The wavelet coefficients' maximum in each sub-band.
(b) The wavelet coefficients' mean in each sub-band.
(c) The wavelet coefficients' minimum in each sub-band.
(d) The wavelet coefficients' standard deviation in each sub-band.

The features (a–c) represent the signal's frequency distribution and the feature (d) represents the number of changes in a frequency distribution. These are the statistical measures used to extract a unique feature from the ultrasonic measurements and were also the neural net inputs for flow recognition [16,24]. For each of the 125 ultrasonic datasets, the mean, maximum, standard deviation, minimum of the wavelet coefficients were derived.

Compared to S.G. Nnabuife et al. [32], the difference of this research is mainly located in the signal processing step before the classification. S. G. Nnabuife et al. [32] applied Twin-Window Feature (TWF) algorithm for the pre-processing. The core technology for the TWF algorithm is the window sliding strategy and Fast Fourier Transformation (FFT). However, this research adopts the wavelet functions and scaling functions-based multi-resolution decomposition as the pre-processing method for the flow regime classification. Although FFT can depict the overall frequency distribution, it FFT inevitably ignores the detailed difference in a local region. That causes difficulty to choose a proper length for window size, and S.G. Nnabuife et al. [32] spend a long context to discuss the window length setting. Wavelet transformation does not have this issue, it's especially good at focusing on the local difference while analysing the overall features.

3.6. Flow regimes classification with neural network

The extracted features from DWT and PSD were fed as inputs into a feedforward neural network for the two-phase gas-liquid flow regimes' classification. The classified flow regimes, which are the network output, are slug, annular flow, bubbly flow, and churn flow. The feature extracted from the 125 datasets is randomly divided into training, validation and testing datasets in the ratio of 0.60:0.15:0.25, as shown in Figs. 6 and 7, where the x-axis labelled 1–4 represents the four flow regimes: 1. slug flow, 2. bubbly flow, 3. churn flow and 4. annular flow. The all-data subplot shows the number of samples collected for each flow regime. The data distribution used in a neural network with features extracted from DWT and PSD is Figs. 6 and 7.

The neural network applied for flow regime classification in this work is comprised of a feedforward network with twenty hidden neurons. The number of hidden neurons were determined by applying fminsearch optimisation over the data given data sets. The hidden layer uses a sigmoid activation function, whereas the output layer uses a softmax activation function. The network has four output neurons, which correspond to the element number in the target vector, as shown in Fig. 8. When features from PSD are applied, the network has 13 inputs, as shown in Fig. 8. However, when DWT features are applied, the network has 40 inputs, as shown in Fig. 9.

The reason for using ANN is that the amount of data used is not large. The ANN network shown in Figs. 8 and 9 is a shallow neural network in machine learning rather than a deep neural network. In other words, it's a machine learning-based model instead of deep learning. The specific reasons are as following:

(i) Deep learning model corresponds to a more sophisticated computational graph than the applied ANN model, which requires big data for training the deep learning model. The dataset used in this research is small (only 125 samples), which is prone to overfitting in deep learning.

Fig. 13. Confusion plot of the PSD features applied in the combined neural network for flow regimes classification.

(ii) Deep learning has more layers in the network. Eq. (16) depicts the calculations with the first layer, while Eq. (17) characterizes the calculations in the n^{th} layer. It can be found that, as the depth of the neural network increases, the gradients propagating in the network become increasingly weaker. This will also decrease the learning efficiency of the network. Furthermore, this weakening can increase the risk of gradient vanishing. In particular, the "sigmoid" activation in the hidden layer has almost zero feedback when x is far away from zero (see Fig. 10). When the depth of the neural network increases, Sigmoid is very prone to gradient vanishing.

$$y_1 = Sigmoid(w_1 * x_1 + b_1) \tag{16}$$

$$y_n = Sigmoid(w_n * Sigmoid(w_{n-1} * [\cdots Sigmoid(w_1 * x_1 + b_1) \cdots] + b_{n-1}) + b_n) \tag{17}$$

During training, the network is attuned according to the error, and the validation dataset is used to measure the network's generalisation. Unlike the validation datasets, the test dataset does not affect the training but provides the performance of the network during and after training [48]. Training is aborted when the generalisation stops improving, as indicated by an increase in the cross-entropy error of the validation samples for up to six consecutive iterations. The classification is improved as the cross-entropy error is minimised and the percentage error indicates the number of misclassified samples. In addition to an increase in cross-entropy error, overfitting is also observed when the performance of the training set is good but that of the test set is significantly worse.

Fig. 11 describes the best validation performance of the network using PSD- and DWT-extracted features, which are represented in Plots A and B, respectively. The validation performance for DWT features

Fig. 14. Confusion plot of the DWT features applied in the combined neural network for flow regimes classification.

(Plot B: 0.068402) shows improvement compared to that for PSD features (Plot A: 0.095211). Discrete wavelet transform was observed to have a lower cross-entropy error and gradient. The classification is improved as the cross-entropy error is minimised. This information is further explained in Fig. 12 using the Receiver Operating Characteristic (ROC) plot. In each axis, the coloured lines represent the ROC curve, which is the false positive rate (1 - specificity) against the true positive rate (sensitivity) plot as the threshold is varied. An accurate test would show points in the upper-left corner, with 100% specificity and 100% sensitivity. For this case study, the network performance was quite good. Subplots A and B show the result obtained using features from PSD and DWT, respectively. Again, the improvement from using the feature from DWT instead of PSD is seen. Discrete wavelet transform features give a minimal false positive rate, showing points in the upper-left corner, with higher specificity and sensitivity percentages. The test data ROC of B gives 100% specificity and sensitivity for all classes except class 1 (slug flow), with 98.6% specificity and 98.6% sensitivity.

Various neural network algorithms were applied during training, including BFGS quasi-Newton, Levenberg-Marquardt (LM), conjugate gradient with Powell/Beale restarts, Fletcher-Powell conjugate gradient, Polak-Ribiére conjugate gradient, one step secant, resilient backpropagation, Variable learning rate backpropagation and scaled conjugate gradient. The Scaled Conjugate Gradient (SCG) produced a superior performance for the flow regime classification compared to other methods.

The conjugate gradient (SCG) algorithms, in particular SCG, perform well across a wide range of problems, particularly for networks with a large number of weights. On pattern recognition and function approximation problems, the SCG algorithm is nearly as efficient as the Resilient Backpropagation (Rprop) algorithm, and it is as quick as the Levenberg-Marquardt (LM) algorithm. When the error is reduced, the SCG performance does not degrade as fast as the Rprop performance. Memory requirements for SCG algorithms are relatively low [49].

In general, for networks with a few hundred weights, the LM algorithm has the quickest convergence based on the function approximation issues [50]. The benefit of LM is usually visible if precise training is

needed. In most senarios, LM can provide lower Mean Square Errors (MSE) than any of the other tested algorithms. However, as the network weight number increases, the LM advantage decreases. Moreover, the performance of LM is relatively poor on pattern recognition problems. The LM storage requirements are more significant than those of the other algorithms tested.

Resilient Backpropagation (Rprop) is the fastest algorithm on pattern recognition problems. However, it does not have good performance on function approximation problems. Its performance decreases as the error goal decreases. The Rprop algorithm's memory requirements are relatively small compared to those of the other algorithms considered [51,52].

The BFG performance is similar to the LM performance. It does not require much storage as LM, but the computation requirement geometrically increases with the network size because the matrix inverse equivalent needs to be estimated at each iteration [53].

The GDX variable's learning rate algorithm is far slower than that of the other methods and its storage requirements are almost equivalent to those of the Rprop, but it can still be useful for certain problems. In several specific situations, it is better to converge more slowly. For instance, in using early stopping, the results can be inconsistent if an algorithm that converges too quickly is used, as the point at which the error on the validation set is minimised might be overshot [53].

The confusion matrix in Figs. 13 and 14 is used to further compare the neural network results obtained by applying features extracted using DWT and PSD, respectively. The diagonal cells present the correctly classified dataset's number and the misclassified datasets are shown in the off-diagonal cells. The total percentage of the correctly classified cases in green and the misclassified cases in red is shown in the blue cell at the bottom right. The confusion matrix shows that in using PSD during testing, 90.7% (28 out of 31) were classified correctly and 9.7% were misclassified (3 out of 31) as depicted in Fig. 13.

Using DWT features, 98.6% were classified correctly (30 out of 31) and 3.2% were misclassified (1 out of 31) as presented in Fig. 14. The information also reveals the flow regime for the misclassified testing data. For instance, from Fig. 13 it can be observed that one dataset from class 1 (slug flow) and two datasets from class 3 (churn flow) were misclassified. Similarly, from Fig. 14 it can be observed that the only misclassified data came from class 1 (slug flow). The trained network misclassified three datasets, the DWT-trained network, on the other hand, misclassified only one data point.

Table 4 presents a summary of the accuracies of the flow regime classification and the classification method used.

4. Results and discussions

A trial was made to classify gas-liquid two-phase flow using an ANN with Doppler ultrasonic signals. The features acquired from the PSD and DWT frequency bands were fed into the neural network as the input, as shown in Fig. 2. Using a neural network, the extracted features were classified into one of the four flow regime categories: the bubbly, slug, churn and annular flow regimes. To improve the neural network flow regime classifier's performance, the number of features or inputs and the number of hidden neurons were increased with caution to avoid overfitting. In addition, the initial network weights and biases of the network were tuned accordingly.

4.1. Feature extractions

Doppler ultrasonic signal features of the flow were extracted using PSD and DWT. The spectral analysis frequency domain of Doppler ultrasonic signals was deployed using PSD based on Fourier transform. The average PSD spectrum was then taken and fed into the neural network as input. It is essential to extract the spectra statistical moments [39]. Ten frequency bands were extracted from the DWT coefficients and 40 features from the 10 DWT coefficient levels were obtained for each of the datasets using the statistical measures deployed to the wavelet levels.

4.2. Flow regime identification

The feature extracted from the 125 datasets was randomly divided into testing, training, and validation datasets in the ratio of 0.60:0.15:0.25. The flow regimes classifier testing was done using 31 datasets (comprised of the four flow regimes), as shown in Figs. 6 and 7. After training and validation using training and validation datasets, the network was tested with the testing datasets that were yet unseen by the network. The result was analysed, after which the testing dataset's classification errors were evaluated using the best validation performance, the ROC plot and a confusion matrix. The neural network results obtained from the features extracted using DWT and PSD were compared. The result obtained from the features extracted using the DWT feedforward neural network showed improvement compared to that obtained using PSD.

5. Conclusion

In this work, Doppler ultrasonic sensor and ANN were developed for the classification of gas-liquid two-phase flow regimes. The Doppler ultrasonic signal was processed using PSD and DWT features' extraction methods for the extraction of input features in the neural network models. Using a neural network, the features extracted were classified into one of the four flow regime categories: the bubbly, slug, churn and annular flow regimes. To improve the performance of the neural network flow regime classifier, the number of inputs or features and hidden neurons were increased with caution to avoid overfitting. Also, the initial network biases and weights of the network were tuned accordingly. On the application of PSD features, the neural network classifier misclassified three out of 31 test datasets in the classification and gave 90.3% accuracy, while with the DWT features only one dataset was misclassified, yielding an accuracy of 96.8% and thus showing the superiority of the DWT in feature extraction of flow regime classification. It is noteworthy that this research can be extended to many future projects. The flow's transient is a difficult scenario to solve because the real-time property must be taken into account. Real-time properties can inevitably lead to the discussion of the balance between real-time and computing power. Recurrent neural network-based technology can manipulate the time-domain signals, which might be a promising idea for the transient.

Declaration of Competing Interest

The authors declared that they have no conflicts of interest to this work. We declare that we do not have any commercial or associative interest that represents a conflict of interest in connection with the work submitted.

References

[1] R. Thorn, G.A. Johansen, B.T. Hjertaker, Three-phase flow measurement in the petroleum industry, Meas. Sci. Technol. 24 (2013) 17, https://doi.org/10.1088/0957-0233/24/1/012003.
[2] K. Yamaguchi, Y. Yamazaki, Characteristics of countercurrent gas-liquid two-phase flow in vertical tubes, J. Nucl. Sci. Technol. 19 (1982) 985–996, https://doi.org/10.1080/18811248.1982.9734247.
[3] M. Firouzi, S. Hashemabadi, Analytical solution for newtonian laminar flow through the concave and convex ducts, J. Fluids Eng. 131 (2009) 1–6, https://doi.org/10.1115/1.3184026.
[4] L. Cheng, G. Ribatski, J.R. Thome, Two-phase flow patterns and flow-pattern maps: fundamentals and applications, Appl. Mech. Rev. 61 (2008), 050802, https://doi.org/10.1115/1.2955990.
[5] M. Al-naser, M. Elshafei, A. Al-sarkhi, Artificial neural network application for multiphase flow patterns detection : a new approach, J. Pet. Sci. Eng. 145 (2016) 548–564, https://doi.org/10.1016/j.petrol.2016.06.029.

[6] S. Bin, H. Zhang, L. Cheng, Y. Zhao, Flow regime identification of gas-liquid two-phase flow based on HHT, Chin. J. Chem. Eng. 14 (2006) 24–30, https://doi.org/10.1016/S1004-9541(06)60033-5.

[7] M. Alssayh, A. Addali, D. Mba, T. Dao, Identification of two phase flow regime using acoustic emission technology, Int. J. Mech. Prod. Eng. 1 (2013) 27–31. CSMEPU-112-227.

[8] S.Z. Rouhani, M.S. Sohal, Two-phase flow patterns: a review of research results, Prog. Nucl. Energy 11 (1983) 219–259, https://doi.org/10.1016/0149-1970(83)90012-4.

[9] J.E. Juliá, Y. Liu, S. Paranjape, M. Ishii, J. Enrique, L. Yang, P. Sidharth, M. Ishii, Upward vertical two-phase flow local flow regime identification, Nucl. Eng. Des. 238 (2008) 156–169, https://doi.org/10.1016/j.nucengdes.2007.05.005.

[10] P.L. Spedding, G.S. Woods, R.S. Raghunathan, J.K. Watterson, Vertical two-phase flow part I: flow regimes, Oil Nat. Gas Prod. 76 (1998) 612–619, https://doi.org/10.1205/026387698525298.

[11] G.F. Hewitt, D.N. Roberts, Studies of two-phase flow patterns by simultaneous X-ray and flash photography, Harwell, Berkshire, 1969. a953138.pdf.

[12] J.E. Julia, B. Ozar, J.J. Jeong, T. Hibiki, M. Ishii, Flow regime development analysis in adiabatic upward two-phase flow in a vertical annulus, Int. J. Heat Fluid Flow. 32 (2011) 164–175, https://doi.org/10.1016/j.ijheatfluidflow.2010.09.003.

[13] N.K. Omebere-Iyari, B.J. Azzopardi, A study of flow patterns for gas/liquid flow in small diameter tubes, Chem. Eng. Res. Des. 85 (2007) 180–192, https://doi.org/10.1205/cherd05059.

[14] S. Cai, H. Toral, J. Qiu, J. Archer, Neural network based objective flow regime identification in air-water two phase flow, Can. J. Chem. Eng. 72 (1994) 440–445, https://doi.org/10.1002/cjce.5450720308.

[15] Y. Mi, M. Ishii, L.H. Tsoukalas, Flow regime identification methodology with neural networks and two-phase flow models, Nucl. Eng. Des. 204 (2001) 87–100, https://doi.org/10.1016/S0029-5493(00)00325-3.

[16] J.Y. Lee, M. Ishii, N.S. Kim, Instantaneous and objective flow regime identification method for the vertical upward and downward co-current two-phase flow, Int. J. Heat Mass Transf. 51 (2008) 3442–3459, https://doi.org/10.1016/j.ijheatmasstransfer.2007.10.037.

[17] D. Winters, K. B, Rouseff, Tomographic reconstruction of stratified fluid flow, IEEE Trans. Ultrason. Ferroelectr. Freq. Control. UFFC-40 40 (1993) 26–33, https://doi.org/10.1109/58.184995.

[18] K. Muvvala, V. Kumar, B.C. Meikap, S. Chakraborty, Development of soft sensor to identify flow regimes in horizontal pipe using digital signal processing technique, Ind. Eng. Chem. Res. 49 (2010) 3001–3010, https://doi.org/10.1021/ie9019215.

[19] A. Ogazi, Y. Cao, H. Yeung, L. Lao, Slug control with large valve openings to maximize oil production, SPE J. 15 (2010) 8–11, https://doi.org/10.2118/124883-PA.

[20] E.S. Rosa, R.M. Salgado, T. Ohishi, N. Mastelari, Performance comparison of artificial neural networks and expert systems applied to flow pattern identification in vertical ascendant gas-liquid flows, Int. J. Multiph. Flow 36 (2010) 738–754, https://doi.org/10.1016/j.ijmultiphaseflow.2010.05.001.

[21] T. Tambouratzis, I. Pázsit, Non-invasive on-line two-phase flow regime identification employing artificial neural networks, Ann. Nucl. Energy 36 (2009) 464–469, https://doi.org/10.1016/j.anucene.2008.12.002.

[22] S.G. Nnabuife, P. Sharma, E. Iyore Aburime, P.L. Lokidor, A. Bello, Development of gas-liquid slug flow measurement using continuous-wave doppler ultrasound and bandpass power spectral density, ChemEngineering 5 (2021) 2, https://doi.org/10.3390/chemengineering5010002.

[23] Z.K. Gao, P.C. Fang, M.S. Ding, N. De Jin, Multivariate weighted complex network analysis for characterizing nonlinear dynamic behavior in two-phase flow, Exp. Therm. Fluid Sci. 60 (2015) 157–164, https://doi.org/10.1016/j.expthermflusci.2014.09.008.

[24] E.D. Übeyli, I. Güler, Improving medical diagnostic accuracy of ultrasound Doppler signals by combining neural network models, Comput. Biol. Med. 35 (2005) 533–554, https://doi.org/10.1016/j.compbiomed.2004.03.006.

[25] D. Kouam, J. Girault, J. Remenieras, High resolution processing techniques for ultrasound doppler velocimetry in the presence of colored noise . Part II : multiplephase pipe-flow velocity measurement, IEEE Trans. Ultrason. Ferroelec. Frequ. Control. 50 (2003) 267–278.

[26] J.L. Goncalves, T.A. Paiva, J.R. Abud Jr, R.D.M. Carvalho, O.J. Venturini, Development of a multiphase flow metering procedure based on the ultrasonic technique, in: 15th International Conference Multiphase Production Technology, BHR Group, Cannes, France, 2011, pp. 101–115.

[27] S. Wada, H. Kikura, M. Aritomi, Pattern recognition and signal processing of ultrasonic echo signal on two-phase flow, Flow Meas. Instrum. 17 (2006) 207–224, https://doi.org/10.1016/j.flowmeasinst.2005.11.006.

[28] S. Fan, T. Yan, Two-phase air-water slug flow measurement in horizontal pipe using conductance probes and neural network, IEEE Trans. Instrum. Meas. 63 (2014) 456–466, https://doi.org/10.1109/TIM.2013.2280485.

[29] E. Weinstein, Measurement of the differential doppler shift, IEEE Trans. Acoust. 30 (1982) 112–117, https://doi.org/10.1109/TASSP.1982.1163849.

[30] X. Dong, C. Tan, Y. Yuan, F. Dong, Oil-water two-phase flow velocity measurement with continuous wave ultrasound Doppler, Chem. Eng. Sci. 135 (2015) 155–165, https://doi.org/10.1016/j.ces.2015.05.011.

[31] R.C. Chivers, C.R. Hill, A spectral approach to ultrasonic scattering from human tissue: methods, objectives and backscattering measurements, Phys. Med. Biol. 20 (1975) 799–815, https://doi.org/10.1088/0031-9155/20/5/009.

[32] S.G. Nnabuife, B. Kuang, J.F. Whidborne, Z. Rana, Non-intrusive classification of gas-liquid flow regimes in an S-shaped pipeline riser using a Doppler ultrasonic sensor and deep neural networks, Chem. Eng. J. 403 (2020), 126401, https://doi.org/10.1016/j.cej.2020.126401.

[33] F.W. Kremkau, Physical principles of ultrasound, Semin. Roentgenol. 10 (1975) 259–263, https://doi.org/10.1016/0037-198X(75)90045-0.

[34] B. Kuang, S.G. Nnabuife, Z. Rana, Pseudo-image-feature-based identification benchmark for multi-phase flow regimes, Chem. Eng. J. Adv. 5 (2021), 100060, https://doi.org/10.1016/j.ceja.2020.100060.

[35] S.G. Nnabuife, K.E.S. Pilario, L. Lao, Y. Cao, M. Shafiee, Identification of gas-liquid flow regimes using a non-intrusive Doppler ultrasonic sensor and virtual flow regime maps, Flow Meas. Instrum. (2019) 68, https://doi.org/10.1016/j.flowmeasinst.2019.05.002.

[36] Y.M. Zhang, H. Wang, J.X. Mao, Z.D. Xu, Y.F. Zhang, Probabilistic framework with bayesian optimization for predicting typhoon-induced dynamic responses of a long-span bridge, J. Struct. Eng. 147 (2021), 04020297, https://doi.org/10.1061/(ASCE)ST.1943-541X.0002881.

[37] H. Stoppiglia, G. Dreyfus, R. Dubois, Y. Oussar, Ranking a random feature for variable and feature selection, J. Mach. Learn. Res. 3 (2003) 1399–1414, https://doi.org/10.1162/153244303322753733.

[38] Z. Shang, R. Yang, X. Cao, Y. Yang, An investigation of two-phase flow instability using wavelet signal extraction technique, Nucl. Eng. Des. 232 (2004) 157–163, https://doi.org/10.1016/j.nucengdes.2004.06.008.

[39] T. Xie, S.M. Ghiaasiaan, S. Karrila, Artificial neural network approach for flow regime classification in gas-liquid-fiber flows based on frequency domain analysis of pressure signals, Chem. Eng. Sci. 59 (2004) 2241–2251, https://doi.org/10.1016/j.ces.2004.02.017.

[40] J.A. Montgomery, H.C. Yeung, The stability of fluid production from a flexible riser, J. Energy Resour. Technol. 124 (2002) 83, https://doi.org/10.1115/1.1467646.

[41] B.M. Abbagoni, Y. Hoi, Non-invasive classification of gas - liquid two-phase horizontal flow regimes using ultrasonic Doppler sensor and neural network, Meas. Sci. Technol. 27 (2016) 1–38, https://doi.org/10.1088/0957-0233/27/8/084002.

[42] J. Drahoš, J. Čermák, Diagnostics of gas-liquid flow patterns in chemical engineering systems, Chem. Eng. Process. Process Intensif. 26 (1989) 147–164, https://doi.org/10.1016/0255-2701(89)90007-X.

[43] A. Subasi, Automatic recognition of alertness level from EEG by using neural network and wavelet coefficients, Expert Syst. Appl. 28 (2005) 701–711, https://doi.org/10.1016/j.eswa.2004.12.027.

[44] A. Cohen, A.J. Kovačević, Wavelets: the mathematical background, Proc. IEEE 84 (1996) 514–522, https://doi.org/10.1109/5.488697.

[45] O. Rioul, M. Vetterli, Wavelets and signal processing, IEEE Signal Process. Mag. 8 (1991) 14–38, https://doi.org/10.1109/79.91217.

[46] M. Saric, L. Bilicic, H. Dujmic, White noise reduction of audio signal using wavelets transform with modified universal threshold, 4th WSEAS Trans, Inf. Sci. Appl. 2 (2005) 279–283.

[47] H. Bendjama, D. Idiou, K. Gherfi, Y. Laib, Selection of wavelet decomposition levels for vibration monitoring of rotating machinery, Ninth Int. Conf. Adv. Eng. Comput. Appl. Sci. Nice France (2015) 96–100, https://doi.org/10.1007/BF01206031.

[48] M. Ferentinou, M. Fakir, Integrating rock engineering systems device and artificial neural networks to predict stability conditions in an open pit, Eng. Geol. 246 (2018) 293–309, https://doi.org/10.1016/j.enggeo.2018.10.010.

[49] M.F. Møller, A scaled conjugate gradient algorithm for fast supervised learning, Neural Netw. 6 (1993) 525–533, https://doi.org/10.1016/S0893-6080(05)80056-5.

[50] T. Sugihara, Solvability-unconcerned inverse kinematics by the levenberg-marquardt method, IEEE Trans. Robot. 27 (2011) 984–991, https://doi.org/10.1109/TRO.2011.2148230.

[51] M. Riedmiller, H. Braun, A direct adaptive method for faster backpropagation learning: The Rprop algorithm, in: Proceedings of the IEEE Nternational Conference on Neural Networks, San Francisco, CA, USA, 1993, pp. 586–591, https://doi.org/10.1109/ICNN.1993.298623.

[52] J. Zhang, P.D. Roberts, On-line process fault diagnosis using neural network techniques, Trans. Inst. Meas. Control. 14 (1992) 179–188, https://doi.org/10.1177/014233129201400402.

[53] J. Ramesh, P.T. Vanathi, K. Gunavathi, Fault classification in phase-locked loops using back propagation neural networks, Electron. Telecommun. Res. Inst. 30 (2008) 546–554, https://doi.org/10.4218/etrij.08.0108.0133.